Journal of Computational Applied Mechanics 2023, 54 (1): 68-86

DOI: 10.22059/JCAMECH.2023.352182.784

RESEARCH PAPER

Shear buckling response of FG porous annular sector plate reinforced by graphene platelet subjected to different shear loads

Mojtaba Khatoonabadi [a], Mohammad Jafari [a], Faraz Kiarasi [b], Mohammad Hosseini [c], Masoud Babaei [d], Kamran Asemi [d, *]

[a] *Faculty of Mechanical and Mechatronics Engineering, Shahrood University of Technology, Semnan, Iran*
[b] *Department of Mechanical Engineering, University of Eyvanekey, Eyvanekey, Semnan, Iran*
[c] *Department of Mechanical Engineering, University of Hormozgan, Bandar Abbas, Iran*
[d] *Mechanical Engineering Department, Islamic Azad University- Tehran North Branch, Tehran, Iran*

Abstract

In this article, shear buckling analysis of functionally graded porous annular sector plate reinforced with graphene nanoplatelets (GPLs) are investigated for the first time. The plate is consisting of a layered model with uniform or non-uniform dispersion of graphene platelets in a metallic matrix including open-cell interior pores. The extended rule of mixture and the modified Halpin-Tsai models and are employed to obtain the effective mechanical properties of the porous nanocomposite plate. Three different porosity distributions in conjunction with five patterns for dispersion of GPL nanofiller are considered through the thickness of plate. Governing equations derived according to the principle of minimum total potential energy based on 3D elasticity theory and generalized geometric stiffness concept. Finally, finite element method is applied for solving the governing equations of structure. The influence of different parameters including various porosity distribution, porosity coefficient, patterns of GPL dispersion, weight fraction of GPL nanofiller, boundary conditions and sector angles on shear buckling loads of the annular sector plate has been surveyed. For instance, by increasing the weight fraction of GPLs, the shear buckling loads of the structure approximately 33% increase.

Keywords: Shear buckling; 3D elasticity theory; Annular sector plate; FEM; FG porous material, GPLs;

1. Introduction

Porous materials, due to their very low density, relatively high stiffness to weight ratio, great specific permeability, high strength and electrical conductivity, have been used in many engineering structures and applications such as in the aerospace, submarine and sea structures. Porous structures have low weight, internal pores and holes in the metal matrix considerably reduce the overall stiffness of structures [1-10]. Consequently, the capacity of these structures subjected to buckling loads isn't so ideal. To compensate for this limitation, reinforcement with GPLs [11-18] into materials with lighter weight is taken into account as a great and useful method to strengthen their mechanical features and increasing their buckling strength. Thus, many investigations have been

[*] Corresponding Authors: k.asemi@iau-tnb.ac.ir (K. Asemi)

performed about the buckling behavior of functionally graded (FG) porous and FG-GPL porous structures. For instance, Kiarasi et al. [19] investigated the buckling analysis of saturated FG porous rectangular plate based on 3D elasticity and by using the finite element- generalized differential quadrature method (FE-GDQM) as novel solution. Babaei et al. [20] applied higher order shear deformation theory (HSDT) and FEM to obtain the critical buckling loads of FG saturated porous beams. Magnucka-Blandzi [21] investigated the problem of axisymmetrical deflection and buckling of circular porous–cellular plate with the geometric model of nonlinear hypothesis. Jabbari et al. [22] presented an analytical solution for buckling analysis of thin circular FG plates made of saturated porous-soft ferromagnetic materials in transverse magnetic field based on classical plate theory (CLPT). A closed form solution for axisymmetric buckling of saturated circular porous-cellular plate based on first-order shear deformation theory was presented by Mojahedin et al. [23]. Mojahedin et al. [24] presented an analytical solution for buckling analysis of functionally graded circular plates made of saturated porous materials based on higher order shear deformation theory. Rezaei and Saidi [25] presented an analytical solution for buckling response of moderately thick fluid-infiltrated porous annular. Rad et al. [26] presented an analytical solution for elastic buckling of fluid infiltrated porous plates based on shear deformation theories. Arshid et al. [27] applied GDQ procedure to investigate the bending and buckling behaviors of heterogeneous temperature-dependent micro annular/circular porous sandwich plates integrated by FGPEM nano-Composite layers based on modified couple stress theory (MCST) in conjunction with first order shear deformation theory (FSDT). Sharifian and Jabbari [28] applied Ritz method to investigate mechanical buckling analysis of saturated porous functionally graded elliptical plates subjected to inplane force resting on two parameters elastic foundation based on HSDT. Zhou et al. [29] presented an accurate nonlinear buckling analysis of FG porous graphene platelet reinforced composite cylindrical shells based on Donnell's shell theory and HSDT. Shahgholian-Ghahfarokhi et al. investigated buckling [30]and torsional buckling [31] analyses of FG porous cylindrical shell reinforced by GPLs based on FSDT and by applying Rayleigh-Ritz method. Based on FSDT and by employing Chebyshev polynomials based Ritz method, buckling response and natural frequencies of FG porous rectangular plates reinforced by GPLs were presented by Yang [32]. Dong [33]presented an analytical solution for buckling of spinning cylindrical shells made of FG-GPL-reinforced porous nanocomposite based on FSDT and by applying Galerkin approach. Ansari et al[34]applied a novel numerical DQ-FEM solution to investigate buckling and post-buckling of FG porous plates reinforced by GPLs with different shapes and boundary conditions. Kitipornchai [35]employed Timoshenko beam to analyze natural frequencies and elastic buckling of FG porous beams reinforced by GPLs by applying Ritz method. Twinkle et al. [36] studied the impact of grading, porosity and non-uniform edge loads on buckling and natural frequency analyses of FG porous cylindrical panel reinforced by GPLs based on HSDT and applying Galerkin method. Nguyen [37] applied a three-variable HSDT and isogeometric analysis (IGA) to investigate natural frequency, buckling and instability analysis of FG porous plates reinforced by GPLs. Based on FSDT, free vibration and buckling behavior of FG porous plates reinforced by GPLs using spectral Chebyshev approach were presented by Rafiei Anamagh and Bediz[38]. Yaghoobi and Taheri [39] presented an analytical solution for buckling analysis of sandwich plates with uniform and non-uniform porous core reinforced with GPLs based on HSDT.

A survey on the previous studies denotes that shear buckling analysis of FG porous annular sector plate reinforced by graphene platelet hasn't been studied so far. Due to the practical application of plate –type structures as a part of complex structures in aerospace industry and possibility of applying shear loads on these components, it is necessary to know the response of these structures made of lightweight material such as FG –GPL porous material under shear loads. Hence, in this research, shear buckling analysis of FG porous annular sector plate reinforced by GPLs is investigated for the first time. The annular sector plate is considered with uniform and non-uniform patterns of GPLs in a metallic matrix containing open-cell internal pores as well as three various porosity distributions that are assumed across the thickness plate including uniform and two types of symmetric functionally graded patterns. In addition, five various patterns of GPL dispersion pattern are assumed through the plate thickness such as: FG GPL-X, A, V, UD and O. 3D elasticity finite element method based on principle of virtual work is applied to obtain governing equations in pre-buckling state. Although 3D elasticity theory consumes more time, it considers thickness stretching unlike other simple shell theories and gives more accurate results. The displacement varies along with the thickness, and it is appropriate for thick structure as same as the structure used in this paper. Shear buckling loads are obtained using nonlinear Green strain tensor and based on a generalized geometric stiffness concept. The effect of different factors such as porosity coefficient, various porosity distributions in conjunction with different GPL patterns, weight fraction of GPLs, sector angle and various boundary conditions on shear buckling loads of FG porous annular sector plate reinforced by GPLs have been investigated.

2. Obtaining the governing equation

2.1. Description of geometry:

An annular sector plate as shown in Fig. 1 is considered. h, R0=a, R1=b and θ0 are thickness, inner radius, outer radius and sector angle of the plate, respectively. r, θ and z are cylindrical coordinate axes, which are located at the mid-plane of the plate. u, v and w are the displacement components of the mid-plane in the r, θ and z directions, respectively.

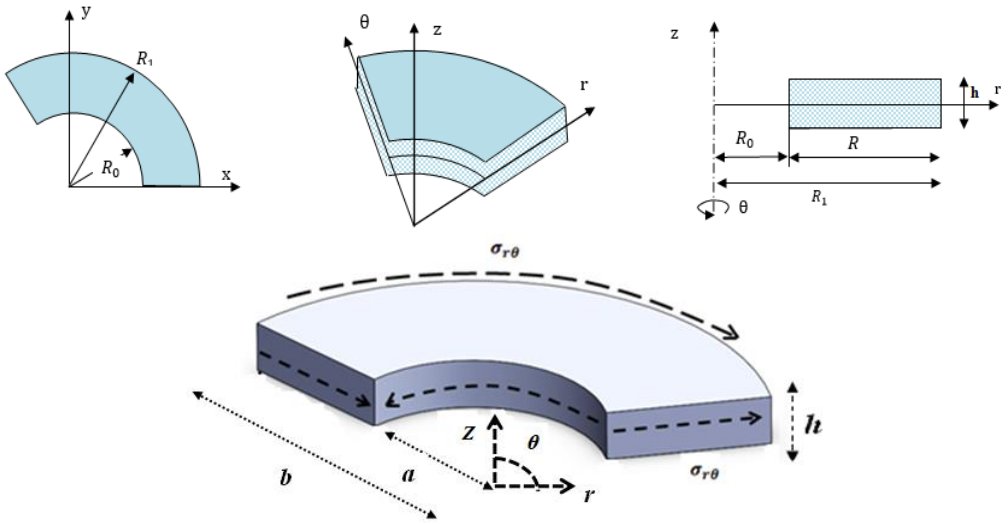

Fig 1: Geometry and coordinate system of porous annular sector plate reinforced by GPLs

2.2. Estimation of effective material properties of porous nanocomposite plates reinforced by GPLs:

Three different porosity distributions are assumed through the plate thickness (Fig. 2). Two kinds of non-uniform symmetric distribution of porosity and a uniform porosity distribution are considered. In distribution 1, the porosity is symmetric nonlinear, and around the mid-plane is higher rather than the upper and lower surfaces. In distribution 2, non-uniform symmetric porosity is considered, and the top and bottom surfaces are higher rather than the mid-plane. The distribution of material properties considering the effect of porosity for distributions 1 and 2 are shown in Eqs. (1) and (2), respectively. The mathematical representation of mechanical properties for the uniform distribution of porosity is shown in Eq. (3). Simultaneously, three GPL distribution patterns along the plate thickness are described in Fig. 2 and given in Eq. (15)[13, 40].

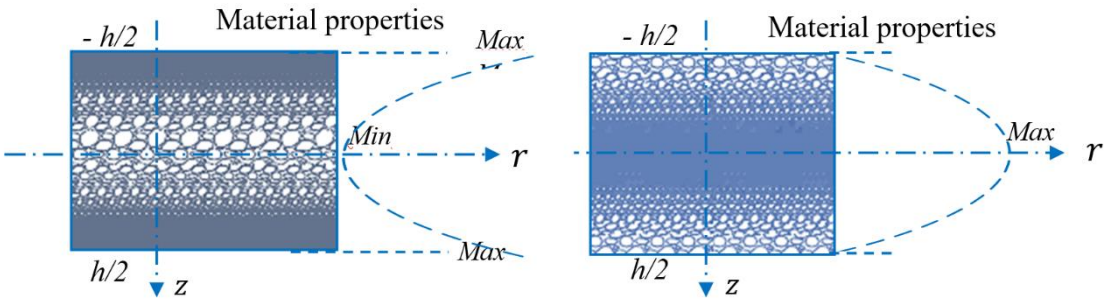

(A) Porosity distribution 1 (symmetric I)

(B) Porosity distribution 2 (symmetric II)

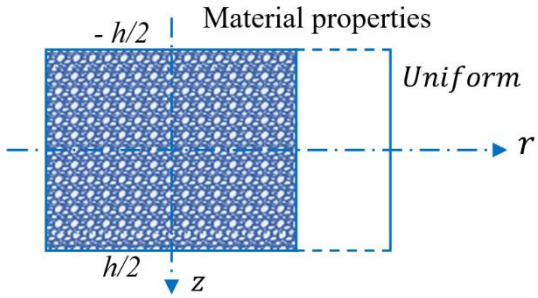

(C) Uniform porosity distribution

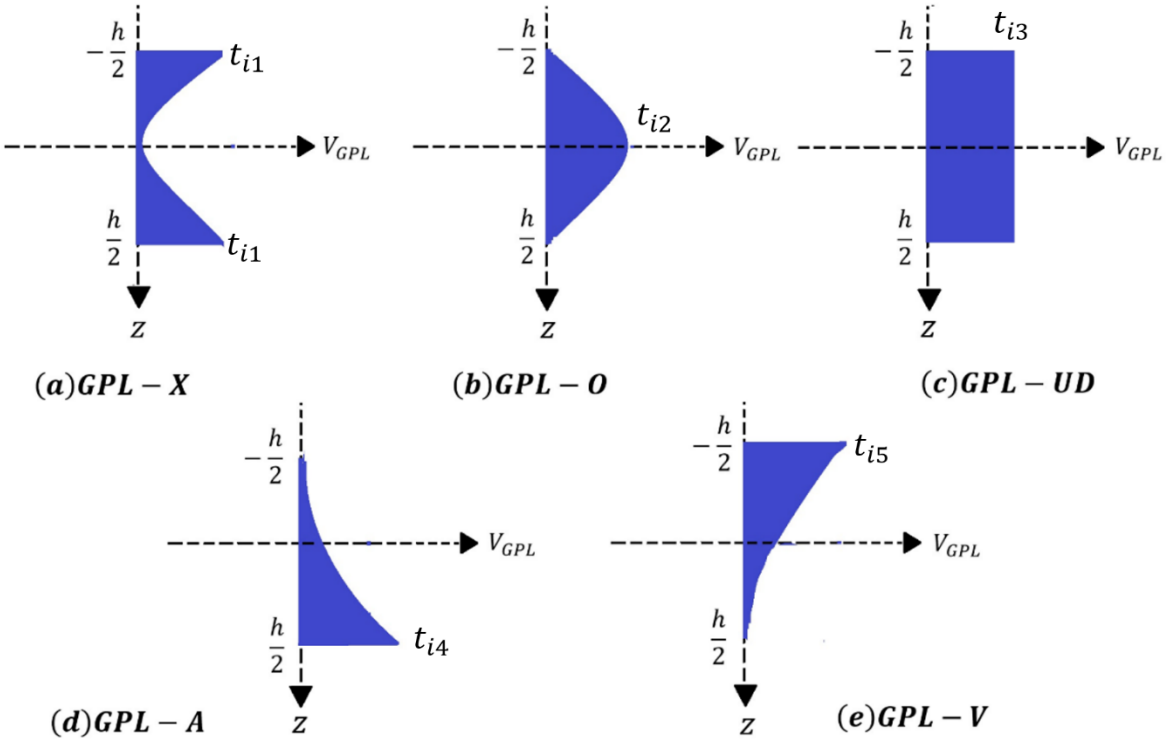

Fig 2: Patterns of porosity and GPL distributions

Porosity distribution 1 (Non-uniform symmetric I):

$$\begin{cases} E(z) = E^* \left[1 - e_0 \cos(\pi z / h)\right] \\ G(z) = G^* \left[1 - e_0 \cos(\pi z / h)\right] \\ \rho(z) = \rho^* \left[1 - e_m \cos(\pi z / h)\right] \end{cases} \quad (1)$$

Porosity distribution 2 (Non-uniform symmetric II):

$$\begin{cases} E(z) = E^* \left[e_0^* \left(1 - \cos(\pi z / h)\right)\right] \\ G(z) = G^* \left[e_0^* \left(1 - \cos(\pi z / h)\right)\right] \\ \rho(z) = \rho^* \left[e_m^* \left(1 - \cos(\pi z / h)\right)\right] \end{cases} \quad (2)$$

Uniform porosity distribution:

$$\begin{cases} E(z) = E^* \alpha \\ G(z) = G^* \alpha \\ \rho(z) = \rho^* \alpha' \end{cases} \quad (3)$$

Where $E(z), G(z)$ and $\rho(z)$ are modulus of elasticity, rigidity modules and mass density of porous nanocomposite plates. E^*, G^* and ρ^* are the same properties of GPL plate without interior cavities. Also, e_0 and $e_0^* (0 \le e_0 (e_0^*) < 1$ are the coefficients of porosity for distribution 1 and 2, respectively. e_m and e_m^* are the corresponding coefficients of mass density for distributions 1 and 2, respectively. α and α' are the variables for uniform porosity distribution. As the size and density of interior cavities increases, the porosity increase, and consequently, causes a decrease in the material properties.

The material properties of open-cell metal foams in Eq. (4) is applied to derive relationship between the porosity coefficients and mass density coefficients for porosity patterns in Eq. (5)

$$\frac{E(z)}{E^*} = \left(\frac{\rho(z)}{\rho^*}\right)^2 \quad (4)$$

$$\begin{cases} 1 - e_m \cos(\pi z / h) = \sqrt{1 - e_0 \cos(\pi z / h)} \\ 1 - e_m^* \left(1 - \cos(\pi z / h)\right) = \sqrt{1 - e_0^* \left(1 - \cos(\pi z / h)\right)} \\ \alpha' = \sqrt{\alpha} \end{cases} \quad (5)$$

The mass of plates with different porosities and GPL dispersions are assumed to be identical, therefore, we have:

$$\begin{cases} \int_0^{h/2} \sqrt{1 - e_0^* \left(1 - \cos(\pi z / h)\right)} dz = \int_0^{h/2} \sqrt{1 - e_0 \cos(\pi z / h)} dz \\ \int_0^{h/2} \sqrt{\alpha} dz = \int_0^{h/2} \sqrt{1 - e_0 \cos(\pi z / h)} dz \end{cases} \quad (6)$$

Which may be applied to estimate e_0^* and α with a known value of e_0, as given in Table 1. It is evident that e_0^* enhances by increasing e_0. When e_0 reaches 0.6, $e_0^* (= 0.9612)$ is near to the upper bound. Thus, $e_0 \in [0, 0.6]$ is applied in the present analyses.

Table 1: Coefficients of porosity for different distributions

e_0	e_0^*	α
0.1	0.1738	0.9361
0.2	0.3442	0.8716
0.3	0.5103	0.8064
0.4	0.6708	0.7404
0.5	0.8231	0.6733
0.6	0.9612	0.6047

Modulus of elasticity of the nanocomposite without interior cavities $E*$ is estimated based on Halpin-Tsai micromechanics model as:

$$E^* = \frac{3}{8}\left(\frac{1+\varepsilon_L^{GPL}\eta_L^{GPL}V_{GPL}}{1-\eta_L^{GPL}V_{GPL}}\right)E_m + \frac{5}{8}\left(\frac{1+\varepsilon_W^{GPL}\eta_W^{GPL}V_{GPL}}{1-\eta_W^{GPL}V_{GPL}}\right) \tag{7}$$

$$\varepsilon_L^{GPL} = \frac{2l_{GPL}}{t_{GPL}} \tag{8}$$

$$\varepsilon_W^{GPL} = \frac{2w_{GPL}}{t_{GPL}} \tag{9}$$

$$\eta_L^{GPL} = \frac{E_{GPL} - E_m}{E_{GPL} + \varepsilon_L^{GPL}E_m} \tag{10}$$

$$\eta_L^{GPL} = \frac{E_{GPL} - E_m}{E_{GPL} + \varepsilon_W^{GPL}E_m} \tag{11}$$

where E_{GPL} and E_m are modulus of elasticity of GPLs and the metallic matrix. l_{GPL}, W_{GPL} and t_{GPL} are length, width and thickness of nanofiller platelets, and V_{GPL} is the volume content of GPLs. The rule of mixture [41]is applied to estimate the mass density and Poisson's ratio of the nanocomposite:

$$\rho^* = \rho_{GPL}V_{GPL} + \rho_m\left(1-V_{GPL}\right) \tag{12}$$

$$v^* = v_{GPL}V_{GPL} + v_m\left(1-V_{GPL}\right) \tag{13}$$

where ρ_{GPL} and v_{GPL} are the mass density and Poisson's ratio of GPLs. ρ_m and υ_m are the same material properties of the metal matrix. Poisson's ratio is assumed to be constant for open-cell metal foams[42-46]. The rigidity modulus $G*$ of the nanocomposite is estimated as:

$$G^* = \frac{E^*}{2\left(1+v^*\right)} \tag{14}$$

The volume content of GPLs V_{GPL} varies through the plate thickness according to the Eq. (15) for various dispersion patterns.

$$V_{GPL}(z) = \begin{Bmatrix} t_{i1}[1-\cos(\pi\zeta)] & GPL-X \\ t_{i2}[\cos(\pi\zeta)] & GPL-O \\ t_{i3} & GPL-UD \\ t_{i4}[1-\cos(\frac{\pi}{4}-\frac{\pi}{2}\zeta)] & GPL-A \\ t_{i5}[\cos(\frac{\pi}{4}-\frac{\pi}{2}\zeta)] & GPL-V \end{Bmatrix} \tag{15}$$

Where $t_{i1}, t_{i2}, t_{i3}, t_{i4}$ and t_{i5} are the upper limit of the V_{GPL}, and i=1, 2, 3 related to different porosity distributions 1, 2 and uniform distribution. The total volume content of GPLs V_{GPL}^T is obtained by using the nanofiller weight fraction Δ_{GPL} in Eq. (16), and then is applied to find S_{i1}, S_{i2} and S_{i3} by Eq. (17).

$$V_{GPL}^{T}=\frac{\Delta_{GPL}\rho_m}{\Delta_{GPL}\rho_m+\rho_{GPL}-\Delta_{GPL}\rho_{GPL}} \tag{16}$$

$$V_{GPL}^{T}\int_{-h/2}^{h/2}\frac{\rho(\zeta)}{\rho^*}d\zeta=\begin{cases}t_{i1}\int_{-h/2}^{h/2}[1-\cos(\pi\zeta)]\dfrac{\rho(\zeta)}{\rho^*}d\zeta\\ t_{i2}\int_{-h/2}^{h/2}[\cos(\pi\zeta)]\dfrac{\rho(\zeta)}{\rho^*}d\zeta\\ t_{i3}\int_{-h/2}^{h/2}\dfrac{\rho(\zeta)}{\rho^*}d\zeta\\ t_{i4}\int_{-h/2}^{h/2}[1-\cos(\dfrac{\pi}{4}-\dfrac{\pi}{2}\zeta)]\dfrac{\rho(\zeta)}{\rho^*}d\zeta\\ t_{i5}\int_{-h/2}^{h/2}[\cos(\dfrac{\pi}{4}-\dfrac{\pi}{2}\zeta)]\dfrac{\rho(\zeta)}{\rho^*}d\zeta\end{cases} \tag{17}$$

2.3. Governing equations of the buckling problem

The constitutive equation of the FG porous annular sector plate reinforced by GPLs assuming the linear elastic behavior for the plate in cylindrical coordinates is as:

$$\boldsymbol{\sigma}=\boldsymbol{D}\boldsymbol{\varepsilon} \tag{18}$$

Where

$$\boldsymbol{\sigma}=\left[\sigma_r,\sigma_\theta,\sigma_z,\tau_{r\theta},\tau_{\theta z},\tau_{rz}\right]^T$$
$$\boldsymbol{\varepsilon}=\left[\varepsilon_r,\varepsilon_\theta,\varepsilon_z,\gamma_{r\theta},\gamma_{\theta z}\,\gamma_{rz}\right]^T \tag{19}$$

Where σ_{ij} and $\varepsilon_{ij}\,(i,j=r,\theta,z)$ are the stress and strain components, respectively. Also, the elasticity matrix D is:

$$\boldsymbol{D}=\frac{E(z)(1-\nu)}{(1+\nu)(1-2\nu)}\begin{pmatrix}1 & \frac{\nu}{1-\nu} & \frac{\nu}{1-\nu} & 0 & 0 & 0\\ \frac{\nu}{1-\nu} & 1 & \frac{\nu}{1-\nu} & 0 & 0 & 0\\ \frac{\nu}{1-\nu} & \frac{\nu}{1-\nu} & 1 & 0 & 0 & 0\\ 0 & 0 & 0 & \frac{1-2\nu}{2(1-\nu)} & 0 & 0\\ 0 & 0 & 0 & 0 & \frac{1-2\nu}{2(1-\nu)} & 0\\ 0 & 0 & 0 & 0 & 0 & \frac{1-2\nu}{2(1-\nu)}\end{pmatrix}=E(z)\Phi \tag{20}$$

Where the linear and non-linear strain- displacement relations in cylindrical coordinates, considering the theory of elasticity are:

$$\boldsymbol{\varepsilon}_L=\begin{Bmatrix} u_{,r} \\ \dfrac{u+v_{,\theta}}{r} \\ w_{,z} \\ \left(\dfrac{u_{,\theta}-v}{r}+v_{,r}\right) \\ \left(v_{,z}+\dfrac{w_{,\theta}}{r}\right) \\ \left(u_{,z}+w_{,r}\right) \end{Bmatrix}, \quad \boldsymbol{\varepsilon}_{NL}=\frac{1}{2}\begin{Bmatrix} \left(u_{,r}\right)^2+\left(v_{,r}\right)^2+\left(w_{,r}\right)^2 \\ \left(\dfrac{u_{,\theta}-v}{r}\right)^2+\left(\dfrac{v_{,\theta}+u}{r}\right)^2+\left(\dfrac{w_{,\theta}}{r}\right)^2 \\ \left(u_{,z}\right)^2+\left(v_{,z}\right)^2+\left(w_{,z}\right)^2 \\ 2\left(u_{,r}\dfrac{u_{,\theta}-v}{r}+v_{,r}\dfrac{v_{,\theta}+u}{r}+\dfrac{w_{,r}w_{,\theta}}{r}\right) \\ 2\left(\dfrac{u_{,\theta}-v}{r}u_{,z}+\dfrac{v_{,\theta}+u}{r}v_{,z}+\dfrac{w_{,z}w_{,\theta}}{r}\right) \\ 2\left(u_{,r}u_{,z}+v_{,r}v_{,z}+w_{,r}w_{,z}\right) \end{Bmatrix} \tag{22}$$

Indicates partial derivative.

The transformations between cylindrical and local coordinates in an annular sector element are:

$$\xi=(2r-a^{(e)}-b^{(e)})/(b^{(e)}-a^{(e)}), \quad \eta=2\theta/\beta^{(e)}, \quad \zeta=2z/h^{(e)} \tag{23}$$

Where the natural coordinates, $-1\le\xi, \eta$ *and* $\zeta\le 1$ are through the r, θ and z directions, respectively. $a^{(e)}, b^{(e)}$, $\beta^{(e)}$ and $h^{(e)}$ are the inner radii, outer radii, sector angle and thickness of each annular sector element.

Hence, the linear part of strain-displacement relations (22) in matrix form is:

$$\boldsymbol{\varepsilon}_L=\Gamma\mathbb{Q} \tag{24}$$

Where

$$\Gamma=\begin{bmatrix} \dfrac{\partial}{\partial\xi}\dfrac{2}{b^{(e)}-a^{(e)}} & 0 & 0 \\ \dfrac{2}{\xi(b^{(e)}-a^{(e)})+a^{(e)}+b^{(e)}} & \dfrac{4}{\xi(b^{(e)}-a^{(e)})+a^{(e)}+b^{(e)}}\dfrac{\partial}{\beta^{(e)}\partial\eta} & 0 \\ 0 & 0 & \dfrac{2\partial}{h^{(e)}\partial\zeta} \\ \dfrac{4}{\xi(b^{(e)}-a^{(e)})+a^{(e)}+b^{(e)}}\dfrac{\partial}{\beta^{(e)}\partial\eta} & \dfrac{\partial}{\partial\xi}\dfrac{2}{b^{(e)}-a^{(e)}}-\dfrac{2}{\xi(b^{(e)}-a^{(e)})+a^{(e)}+b^{(e)}} & 0 \\ 0 & \dfrac{2\partial}{h^{(e)}\partial\zeta} & \dfrac{4}{\xi(b^{(e)}-a^{(e)})+a^{(e)}+b^{(e)}}\dfrac{\partial}{\beta^{(e)}\partial\eta} \\ \dfrac{2\partial}{h^{(e)}\partial\zeta} & 0 & \dfrac{\partial}{\partial\xi}\dfrac{2}{b^{(e)}-a^{(e)}} \end{bmatrix} \tag{25}$$

$$\mathbb{Q}=\begin{Bmatrix} u \\ v \\ w \end{Bmatrix} \tag{26}$$

Here, a three dimensional graded FEM is developed for buckling problem of FG porous annular sector plates reinforced by GPLs. Three–dimensional 8- node solid graded elements are selected for discretization of the domain. In contrast to the conventional solid elements, material properties are also considered as nodal degrees of freedom. Following the conventional FEM, the displacement vector $\mathbb{Q}$ of an arbitrary point of the element may be associated with the nodal displacement vectors of the element $\Delta^{(e)}$ by applying the shape function matrix N, as

$$\mathbb{Q}=\boldsymbol{N}\,\Delta^{(e)} \tag{27}$$

Where

$$\Delta^{(e)}=\{U_1 \;\; V_1 \;\; W_1 \;\; . \;\; . \;\; . \;\; U_8 \;\; V_8 \;\; W_8\}^{\mathbf{T}} \tag{28}$$

$$\boldsymbol{N}=\begin{bmatrix} N_1 & 0 & 0 & N_2 & 0 & 0 & \dots & N_8 & 0 & 0 \\ 0 & N_1 & 0 & 0 & N_2 & 0 & \dots & 0 & N_8 & 0 \\ 0 & 0 & N_1 & 0 & 0 & N_2 & \dots & 0 & 0 & N_8 \end{bmatrix}_{3*24} \tag{29}$$

The components of the shape function matrix may be determined in terms of the natural coordinates as[47]:

$$N_i(\xi,\eta,\zeta)=\frac{1}{8}(1+\xi_i\xi)(1+\eta_i\eta)(1+\zeta_i\zeta) \tag{30}$$

where ξ_i, is the value of the natural coordinate ξ related to the i-th node, e.g., if the i-th node has the coordinates (1,-1,-1), one has: $(\xi_i=1,\eta_i=-1,\zeta_i=-1)$.

In addition, the displacement field, the nonhomogeneity of the material properties of the FG porous plate reinforced by GPLs may also be determined based on their nodal values. Therefore, a graded finite element method may be applied to effectively trace continuous variations of the material properties at the element level. Using the graded elements for modelling gradation of the material properties gives more accurate results than dividing the solution domain into homogenous elements. Hence, shape functions similar to those of the displacement field may be used:

$$E=\sum_{i=1}^{8}E_i\ N_i=\mathbb{N}\boldsymbol{\Xi}\quad,\quad \mathbb{N}=\begin{bmatrix}N_1 & \dots & N_8\end{bmatrix}_{1*8}\quad,\quad \boldsymbol{\Xi}=\begin{bmatrix}E_1 & \dots & E_8\end{bmatrix}^T_{1*8} \tag{31}$$

Where E_i is the Young modulus of elasticity corresponding to node i. $\mathbb{N}$ and $\boldsymbol{\Xi}$ are vectors of shape functions and modulus of elasticity of each element.

Therefore, Eq. (20) can be rewritten as:

$$\boldsymbol{D}=\Phi\mathbb{N}\boldsymbol{\Xi} \tag{32}$$

Substituting (27) into (24) gives the linear part of strain matrix of each element as:

$$\boldsymbol{\varepsilon}_L^{(e)}=\Gamma\boldsymbol{N}\Delta^{(e)}=\mathcal{B}\Delta^{(e)} \tag{33}$$

Where

$$\mathcal{B}=\begin{pmatrix} \dfrac{\xi_1(1+\eta_1\eta)(1+\zeta_1\zeta)}{4(b^{(e)}-a^{(e)})} & 0 & 0 & \dots \\ \dfrac{(1+\xi_1\xi)(1+\eta_1\eta)(1+\zeta_1\zeta)}{4(\xi(b^{(e)}-a^{(e)})+a^{(e)}+b^{(e)})} & \dfrac{\eta_1(1+\xi_1\xi)(1+\zeta_1\zeta)}{2\beta^{(e)}(\xi(b^{(e)}-a^{(e)})+a^{(e)}+b^{(e)})} & 0 & \dots \\ 0 & 0 & \dfrac{\zeta_1(1+\xi_1\xi)(1+\eta_1\eta)}{4h^{(e)}} & \dots \\ \dfrac{\eta_1(1+\xi_1\xi)(1+\zeta_1\zeta)}{2\beta^{(e)}(\xi(b^{(e)}-a^{(e)})+a^{(e)}+b^{(e)})} & \dfrac{\xi_1(1+\eta_1\eta)(1+\zeta_1\zeta)}{4(b^{(e)}-a^{(e)})}-\dfrac{(1+\xi_1\xi)(1+\eta_1\eta)(1+\zeta_1\zeta)}{4(\xi(b^{(e)}-a^{(e)})+a^{(e)}+b^{(e)})} & 0 & \dots \\ 0 & \dfrac{\zeta_1(1+\xi_1\xi)(1+\eta_1\eta)}{4h^{(e)}} & \dfrac{\eta_1(1+\xi_1\xi)(1+\zeta_1\zeta)}{2\beta^{(e)}(\xi(b^{(e)}-a^{(e)})+a^{(e)}+b^{(e)})} & \dots \\ \dfrac{\zeta_1(1+\xi_1\xi)(1+\eta_1\eta)}{4h^{(e)}} & 0 & \dfrac{\xi_1(1+\eta_1\eta)(1+\zeta_1\zeta)}{4(b^{(e)}-a^{(e)})} & \dots \end{pmatrix}_{6*24} \tag{34}$$

Governing equations of the graded elements can be derived based on the principle of minimum total potential energy:

$$\delta\Pi=\delta U-\delta W=0 \tag{35}$$

Where U and W are the strain energy and work done by the externally in- plane shear loads, respectively:

$$\delta U = \int_V \delta \boldsymbol{\varepsilon}^T \boldsymbol{\sigma} dV$$
$$\delta W = \left(\int_S \hat{\tau}_{r\theta} v \, dS \right)_{r=a,\, b} + \left(\int_S \hat{\tau}_{\theta r} u \, dS \right)_{\theta=-0,\, \beta^{(e)}} \tag{36}$$

$\hat{\tau}_{r\theta}$ is the externally in- plane shear loads of the edges. V and S are the volume and boundary surface of the element, respectively. In the pre-buckling state, the displacement components may be considered to be small. Therefore, one may write:

$$\delta U = \int_V \delta \boldsymbol{\varepsilon}^T \boldsymbol{\sigma} dV = \delta \Delta^{(e)T} \left(\int_V \mathbb{N} \boldsymbol{\Xi} \mathcal{B}^T \Phi \mathcal{B} \, dV \right) \Delta^{(e)} = \delta \Delta^{(e)T} \boldsymbol{\kappa} \Delta^{(e)} \tag{37}$$

To develop the governing equations of the instability, one may use the following equation that relates the condition of the buckling onset to that of the pre-buckling state:

$$\delta(\delta \Pi) = \delta^2 \Pi = 0 \tag{38}$$

Therefore, based on Eqs. (37) and (38):

$$\delta \Delta^{(e)T} \boldsymbol{\kappa} \delta \Delta^{(e)} + \delta^2 \Pi_{Ext.} = 0 \tag{39}$$

Based on Eq. (21), the strain energy of the annular sector plate includes linear as well as nonlinear terms of the strain-displacement relations:

$$U = \frac{1}{2} \left(\int_V \boldsymbol{\varepsilon}^T \boldsymbol{\sigma} dV \right) = \frac{1}{2} \left[\int_V \left(\boldsymbol{\varepsilon}_L + \boldsymbol{\varepsilon}_{NL} \right)^T \boldsymbol{\sigma} dV \right] \tag{40}$$

In the pre-buckling state, transverse displacement or large deformations are small. Based on this assumption, only the linear terms of strain- displacement relations appear. Since slope of the plate is not negligible at the buckling occurrence, the nonlinear components of the strain-displacement relations have to be considered. On the other hand, from Eq. (35) or from the principle of minimum total potential energy:

$$\delta(U - W) = 0 \tag{41}$$

Therefore, the following relation appears only after buckling occurrence:

$$U = \Pi_{Ext.} = \tfrac{1}{2} \int_V \left(\boldsymbol{\varepsilon}^{nl} \right)^T \boldsymbol{\sigma} dV$$
$$= \tfrac{1}{2} \int_V \left(\gamma_{r\theta}{}^{nl} \right)^T \tau_{r\theta} dV \tag{42}$$

Since in the beginning of the buckling occurrence:

$$\sigma_{ij} = \hat{\sigma}_{ij} \tag{43}$$

At the boundaries of the plate, Eq. (42) may be rewritten in the following expanded relation, based on Eq. (22):

$$U = \Pi_{Ext.} = \frac{1}{4} \int_V \Psi^T \Theta \Psi dV \tag{44}$$

Where

$$\Psi^T = \left\langle u_{,r} \quad \frac{u_{,\theta} - v}{r} \quad v_{,r} \quad \frac{v_{,\theta} + u}{r} \quad w_{,r} \quad 1/r\, w_{,\theta} \right\rangle = \Delta^{(e)T} \mathbf{\Lambda}$$

$$\Theta = \begin{bmatrix} 0 & \hat{\tau}_{r\theta} & 0 & 0 & 0 & 0 \\ \hat{\tau}_{r\theta} & 0 & 0 & 0 & 0 & 0 \\ 0 & 0 & 0 & \hat{\tau}_{r\theta} & 0 & 0 \\ 0 & 0 & \hat{\tau}_{r\theta} & 0 & 0 & 0 \\ 0 & 0 & 0 & 0 & 0 & \hat{\tau}_{r\theta} \\ 0 & 0 & 0 & 0 & \hat{\tau}_{r\theta} & 0 \end{bmatrix},$$

$$\mathbf{\Lambda} = \begin{pmatrix} \frac{\xi_1(1+\eta_1\eta)(1+\zeta_1\zeta)}{4(b^{(e)}-a^{(e)})} & \frac{\eta_1(1+\xi_1\xi)(1+\zeta_1\zeta)}{2\beta^{(e)}(\xi(b^{(e)}-a^{(e)})+a^{(e)}+b^{(e)})} & 0 & \frac{(1+\xi_1\xi)(1+\eta_1\eta)(1+\zeta_1\zeta)}{4(\xi(b^{(e)}-a^{(e)})+a^{(e)}+b^{(e)})} & 0 & 0 \\ 0 & -\frac{(1+\xi_1\xi)(1+\eta_1\eta)(1+\zeta_1\zeta)}{4(\xi(b^{(e)}-a^{(e)})+a^{(e)}+b^{(e)})} & \frac{\xi_1(1+\eta_1\eta)(1+\zeta_1\zeta)}{4(b^{(e)}-a^{(e)})} & \frac{\eta_1(1+\xi_1\xi)(1+\zeta_1\zeta)}{2\beta^{(e)}(\xi(b^{(e)}-a^{(e)})+a^{(e)}+b^{(e)})} & 0 & 0 \\ 0 & 0 & 0 & 0 & \frac{\xi_1(1+\eta_1\eta)(1+\zeta_1\zeta)}{4(b^{(e)}-a^{(e)})} & \frac{\eta_1(1+\xi_1\xi)(1+\zeta_1\zeta)}{2\beta^{(e)}(\xi(b^{(e)}-a^{(e)})+a^{(e)}+b^{(e)})} \\ \vdots & \vdots & \vdots & \vdots & \vdots & \vdots \\ \frac{\xi_8(1+\eta_8\eta)(1+\zeta_8\zeta)}{4(b^{(e)}-a^{(e)})} & \frac{\eta_1(1+\xi_8\xi)(1+\zeta_8\zeta)}{2\beta^{(e)}(\xi(b^{(e)}-a^{(e)})+a^{(e)}+b^{(e)})} & 0 & \frac{(1+\xi_8\xi)(1+\eta_8\eta)(1+\zeta_8\zeta)}{4(\xi(b^{(e)}-a^{(e)})+a^{(e)}+b^{(e)})} & 0 & 0 \\ 0 & -\frac{(1+\xi_8\xi)(1+\eta_8\eta)(1+\zeta_8\zeta)}{4(\xi(b^{(e)}-a^{(e)})+a^{(e)}+b^{(e)})} & \frac{\xi_8(1+\eta_8\eta)(1+\zeta_8\zeta)}{4(b^{(e)}-a^{(e)})} & \frac{\eta_1(1+\xi_8\xi)(1+\zeta_8\zeta)}{2\beta^{(e)}(\xi(b^{(e)}-a^{(e)})+a^{(e)}+b^{(e)})} & 0 & 0 \\ 0 & 0 & 0 & 0 & \frac{\xi_8(1+\eta_8\eta)(1+\zeta_8\zeta)}{4(b^{(e)}-a^{(e)})} & \frac{\eta_8(1+\xi_8\xi)(1+\zeta_8\zeta)}{2\beta^{(e)}(\xi(b^{(e)}-a^{(e)})+a^{(e)}+b^{(e)})} \end{pmatrix} \tag{45}$$

or:

$$\Pi_{Ext.} = \tfrac{1}{4}\int_V \Psi^T \Theta \Psi\, dV = \tfrac{1}{4}\Delta^{(e)\mathrm{T}} \left(\int_V \mathbf{\Lambda}^T \Theta \mathbf{\Lambda} dV \right) \Delta^{(e)} \tag{46}$$

Therefore, based on Eqs. (39) and (46):

$$\delta^2\Pi = \delta\Delta^{(e)T} \boldsymbol{\kappa}\, \delta\Delta^{(e)} + \delta\Delta^{(e)T} \left(\int_V \mathbf{\Lambda}^T \Theta \mathbf{\Lambda} dV \right) \delta\Delta^{(e)} = 0 \tag{47}$$

or in the following form:

$$\delta\Delta^{(e)\mathrm{T}} \left(\boldsymbol{\kappa} + \boldsymbol{\kappa}_{\boldsymbol{G}} \right) \delta\Delta^{(e)} = 0 \tag{48}$$

$\boldsymbol{\kappa}_{\boldsymbol{G}}$ is the geometric stiffness matrix. Considering that $\delta\Delta^{(e)} \neq \mathbf{0}$, the following governing equation of instability is obtained from Eq. (48):

$$\left(\boldsymbol{\kappa} + \boldsymbol{\kappa}_{\boldsymbol{G}} \right) \delta\Delta^{(e)} = \mathbf{0} \tag{49}$$

Existence of nonzero solution necessitates that the following determinant to be zero:

$$\left| \boldsymbol{\kappa} + \boldsymbol{\kappa}_{\boldsymbol{G}} \right| = \mathbf{0} \tag{50}$$

The load amplification factor may be considered as:

$$\tau_{r\theta}^{Cr} = \lambda_{\mathrm{Cr}}\, \hat{\tau}_{r\theta} \tag{51}$$

Hence, based on Eqs. (37, 47, 50):

$$\left| \int_V \mathbb{N} \Xi \mathcal{B}^T \Phi \mathcal{B} dV + \lambda_{\mathrm{Cr}} \int_V \mathbf{\Lambda}^T \Theta \mathbf{\Lambda} dV \right| = 0,$$
$$dV = \frac{\beta^{(e)} h^{(e)}}{8} (\xi(b^{(e)} - a^{(e)}) + a^{(e)} + b^{(e)})\, d\xi\, d\eta\, d\zeta \tag{52}$$

or in a compact form:

$$F(\lambda_{Cr})=0 \tag{53}$$

3. Results and discussions

In the present section, shear buckling analysis of FG porous annular sector plates for various porosity coefficients, porosity distribution, dispersion of GPLs nanofiller, weight fraction of nanofiller, sector angles, aspect ratio and thickness ratio is presented and discussed in detail.

Hence, the following material properties and geometrical parameters are considered:

Geometry: a=0.25 m, b=0.3 m and $\theta_0=60^\circ,90^\circ,120^\circ$

Material property: $E_m=130GPa$, $\rho_m=8960\frac{kg}{m^3}$, $\upsilon_m=0.34$ for copper, and $E_{GPL}=1.01TPa$, $\rho_{GPL}=1062.5\frac{kg}{m^3}$, $\upsilon_{GPL}=0.186$, $w_{GPL}=1.5\mu m$, $l_{GPL}=2.5\mu m$, $t_{GPL}=1.5nm$ for GPLs.

In this study, three different types of boundary and loading conditions are considered. These boundary condition and their relevant mathematical interpretations are:

a) Plate with movable simply supported edges subjected to shear load at all edges:

$$\begin{aligned} &r=a,b:\ u,w=0,\ \tau_{r\theta}=1(Pa),\\ &\theta=0,\beta:\ v,w=0,\ \tau_{r\theta}=1(Pa) \end{aligned} \tag{54}$$

b) Plate with immovable simply supported radial edges and free circumferential edges subjected to two anti-phase shear loads at circumferential edges:

$$\begin{aligned} &\theta=0,\beta:\ u,v,w=0,\\ &r=a,b:\tau_{r\theta}=1(Pa) \end{aligned} \tag{55}$$

c) Plate with immovable simply supported circumferential edges and free radial edges subjected to two anti-phase shear loads at radial edges:

$$\begin{aligned} &r=a,b:\ u,v,w=0,\\ &\theta=0,\beta:\tau_{r\theta}=1(Pa) \end{aligned} \tag{56}$$

3.1. Validation of the present study

To verification of the present study, a comparison study is performed. Present results for the critical shear buckling load of homogenous annular sector plate for various boundary conditions and sector angles are compared with those extracted from a well-known commercial finite element analysis code (ANSYS), in Table 1. For this target, it is sufficient to consider the weight fraction of GPL nanofiller and porosity coefficient in MATLAB code equal zero. In this way, porous nanocomposite annular sector plate is changed to a homogenous annular sector plate. As can be seen from Table 1, there is an excellent agreement between the present study and ANSYSWORKBENCH software. The geometry and mechanical properties are assumed as the following:

Mechanical property: $E_m=130GPa$, $\upsilon_m=0.34$

Geometry: $a=0.5m, b=1m$ and $h=0.1m$.

Table 2: Critical buckling loads (GPa) of homogenous annular sector plate for different boundary conditions and sector angles compared with ANSYS (a=0.5 m, b=1 m and h=0.1 m)

Sector angle	$\beta=60^\circ$		$\beta=90^\circ$		$\beta=120^\circ$	
Type of loading and boundary condition	Ansys	Present	Ansys	Present	Ansys	Present
a	13.74	13.70	8.99	8.91	6.34	6.30
b	2.34	2.29	1.98	11.87	0.98	0.94
c	10.87	10.61	11.86	11.74	11.49	11.30

3.2. The results of Shear buckling of FG porous annular sector plate reinforced by GPLs

The effect of various porosity distribution, boundary conditions and sector angles on shear buckling loads of FG porous annular sector plate reinforced by graphene platelet is shown in Table 2. (a=0.5 m, b=1 m and h=0.1 m ,e0=0.5, GPL-X, $\gamma = 0.01wt\%$). As can be seen from this table, the maximum shear buckling loads of structure is belong to PD1,PD2 and PD3, respectively. Also movable simply supported boundary condition has the highest shear buckling loads due to providing more rigidity. It is obvious that by increasing the sector angle, shear buckling loads considerably decrease. The influence of different porosity coefficient on shear buckling loads of structure is given in Table 3(a=0.5 m, b=1 m and h=0.1 m, GPLX, $\gamma = 0.01wt\%$, $\beta = 60^\circ$, PD1) . By increasing the porosity coefficient, the shear buckling loads of structures decrease due to by increasing the porosity coefficient, the stiffness of structure decreases. By comparison of Table 2 and Table 3 , it is clear that the impact of porosity distribution on shear buckling load is greater than porosity coefficient. The influences of various weight fraction of GPL nanofiller on shear buckling loads are indicated in Table 4 (a=0.5 m, b=1 m and h=0.1 m, $\beta = 60^\circ$, e0=0.5, GPL-X, PD1). The impact of the weight fraction of GPL nanofiller plays an important role in stiffness of structure. By adding 1% wt of nanofiller, the shear buckling loads increase approximately 33% and its reason is related to the stiffness of structures. On the other hand, the nano-fillers with high strength and too low weight such as GPLs can significantly improve the stiffness of structures. The effects of various pattern of GPLs dispersion is reported in Table 5 (a=0.5 m, b=1 m and h=0.1 m, e0=0.5, $\beta = 60^\circ$, $\gamma = 0.01wt\%$, PD1). It can be seen that the maximum shear buckling load is related to GPLX. Also shear buckling loads of GPL-A and GPL-V is approximately same. The minimum of shear buckling loads belong to GPL-UD. It is obvious from the results; the maximum influence on shear buckling load is related to weight fraction of nanofiller, GPL pattern, porosity distribution and porosity coefficient, respectively. This problem could significantly help the engineers in their design. The first four shear mode shapes of FG porous annular sector plate reinforced by graphene platelet for various boundary conditions are shown in Figure 3 to 5, respectively.

Table 3: First four shear buckling loads of FG porous annular sector plate reinforced by graphene platelet for different boundary conditions, porosity distribution and sector angles (a=0.5 m, b=1 m and h=0.1 m, e0=0.5, GPL-X)

		$\beta = 60^\circ$			$\beta = 90^\circ$			$\beta = 120^\circ$		
Type of boundary conditions	Buckling load (GPa)	PD1	PD2	PD3	PD1	PD2	PD3	PD1	PD2	PD3
Movable simply supported	Mode 1	19.82	19.35	18.12	12.35	11.86	10.47	8.74	8.55	7.98
	Mode 2	22.54	21.78	18.88	16.81	15.42	13.45	9.12	9.01	8.34
	Mode 3	23.29	22.09	19.31	17.35	16.99	15.13	9.74	8.83	8.69
	Mode 4	26.81	25.87	20.05	20.01	18.68	16.50	10.38	9.73	9.02
Immovable edges at r=a, b	Mode 1	16.86	16.53	15.30	16.93	16.22	15.18	17.09	16.88	15.92
	Mode 2	17.01	16.89	16.00	17.24	16.74	16.67	17.44	16.90	16.34
	Mode 3	20.22	18.28	17.68	21.00	20.86	18.81	21.87	21.33	20.55
	Mode 4	21.00	19.85	18.18	22.35	21.87	19.93	24.18	23.75	21.93
Immovable edges at $\theta = 0, \beta$	Mode 1	2.86	2.78	2.01	1.01	0.91	0.84	0.33	0.3	0.18
	Mode 2	3.90	3.37	3.01	2.87	2.79	1.55	1.12	1.00	0.74
	Mode 3	8.88	7.96	6.64	4.23	3.91	2.33	2.88	1.98	1.29
	Mode 4	10.12	9.99	8.92	8.49	8.10	4.74	3.56	2.84	2.01

Table 4: First four shear buckling loads of FG porous annular sector plate reinforced by graphene platelet for different boundary conditions, porosity coefficient (a=0.5 m, b=1 m and h=0.1 m, GPLX, $\gamma = 0.01wt\%, \beta = 60^o$, PD1)

Type of boundary conditions	Buckling load (GPa)	e0=0.5	e0=0.25	e0=0.1
Movable simply supported	Mode 1	19.82	19.61	19.00
	Mode 2	22.54	21.94	20.12
	Mode 3	23.29	22.88	20.55
	Mode 4	26.81	26.12	25.37
Immovable edges at r=a, b	Mode 1	16.86	16.63	15.89
	Mode 2	17.01	16.90	16.18
	Mode 3	20.22	19.31	18.38
	Mode 4	21.00	20.12	19.10
Immovable edges at $\theta = 0, \beta$	Mode 1	2.86	2.80	2.34
	Mode 2	3.90	3.66	3.22
	Mode 3	8.88	8.12	7.89
	Mode 4	10.12	10.01	9.72

Table 5: First four shear buckling loads of FG porous annular sector plate reinforced by graphene platelet for different boundary conditions, Weight fraction of GPL (a=0.5 m, b=1 m and h=0.1 m ,e0=0.5,GPL-X, $\beta = 60^\circ$,PD1)

Type of boundary conditions	Buckling load (GPa)	$\gamma = 0.01\% wt$	$\gamma = 0.005wt\%$	$\gamma = 0\% wt$
Movable simply supported	Mode 1	19.82	17.61	15.14
	Mode 2	22.54	19.81	17.12
	Mode 3	23.29	20.01	18.35
	Mode 4	26.81	22.66	20.47
Immovable edges at r=a, b	Mode 1	16.86	13.73	11.92
	Mode 2	17.01	14.26	12.99
	Mode 3	20.22	16.13	15.65
	Mode 4	21.00	18.68	16.28
Immovable edges at $\theta = 0, \beta$	Mode 1	2.86	2.00	1.69
	Mode 2	3.90	2.91	2.55
	Mode 3	8.88	6.54	5.86
	Mode 4	10.12	8.00	7.12

Table 6: First four shear buckling loads of FG porous annular sector plate reinforced by graphene platelet for different boundary conditions, and various GPL pattern. (a=0.5 m, b=1 m and h=0.1 m ,e0=0.5, $\beta = 60^{\circ}, \gamma = 0.01wt\%$, ,PD1)

Type of boundary conditions	Buckling load (GPa)	GPL-X	GPL-O	GPL-V	GPL-A	GPL-UD
Movable simply supported	Mode 1	19.82	18.33	17.18	17.14	16.14
	Mode 2	22.54	21.20	19.33	19.28	18.86
	Mode 3	23.29	22.21	21.87	21.79	19.01
	Mode 4	26.81	24.88	23.66	23.61	22.33
Immovable edges at r=a, b	Mode 1	16.86	15.71	13.12	13.06	13.14
	Mode 2	17.01	15.96	13.87	13.81	14.01
	Mode 3	20.22	19.84	17.38	17.31	16.77
	Mode 4	21.00	19.58	17.63	17.59	17.88
Immovable edges at $\theta = 0, \beta$	Mode 1	2.86	2.10	1.88	1.82	1.85
	Mode 2	3.90	3.33	2.79	2.70	2.87
	Mode 3	8.88	7.99	6.64	6.60	6.78
	Mode 4	10.12	9.10	8.47	8.42	8.32

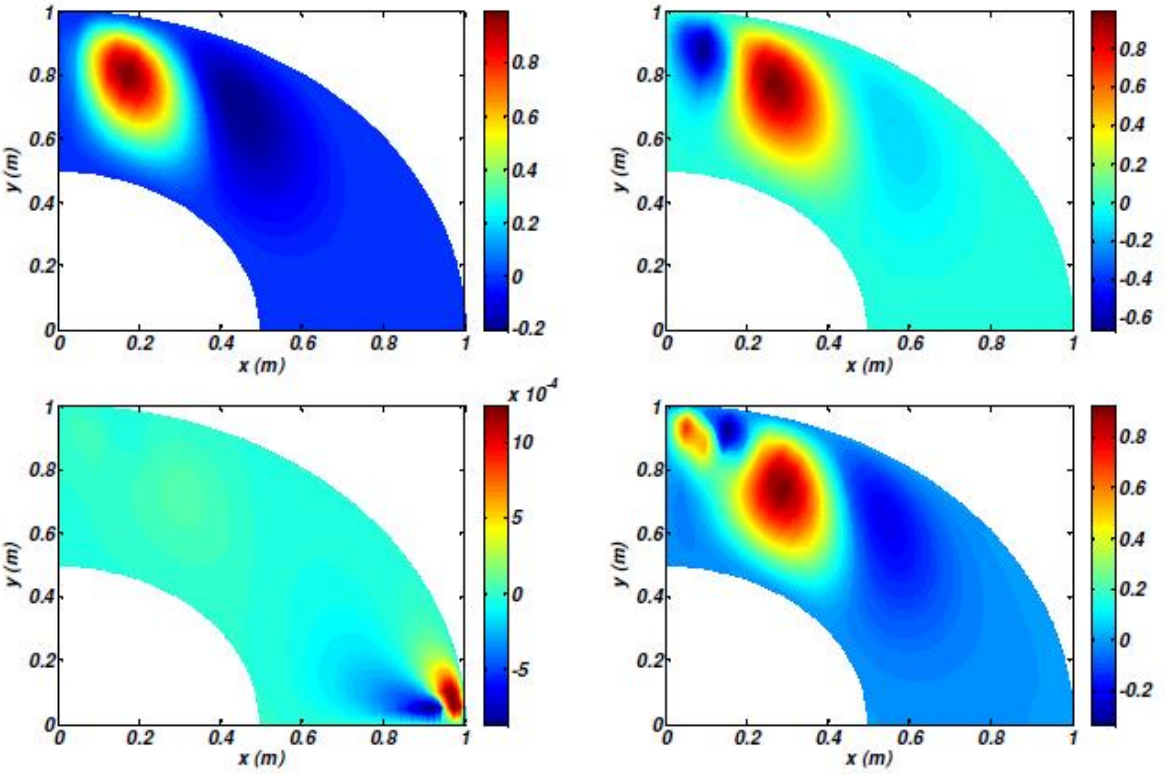

Fig 3: The first four shear mode shapes of FG porous annular sector plate reinforced by graphene platelet (a=0.5m, b=1m and h=0.1m, e_0=0.5, GPL-X, $\beta = 90^{\circ}, \gamma = 0.01\% wt$ PD1 ,B.C.1)

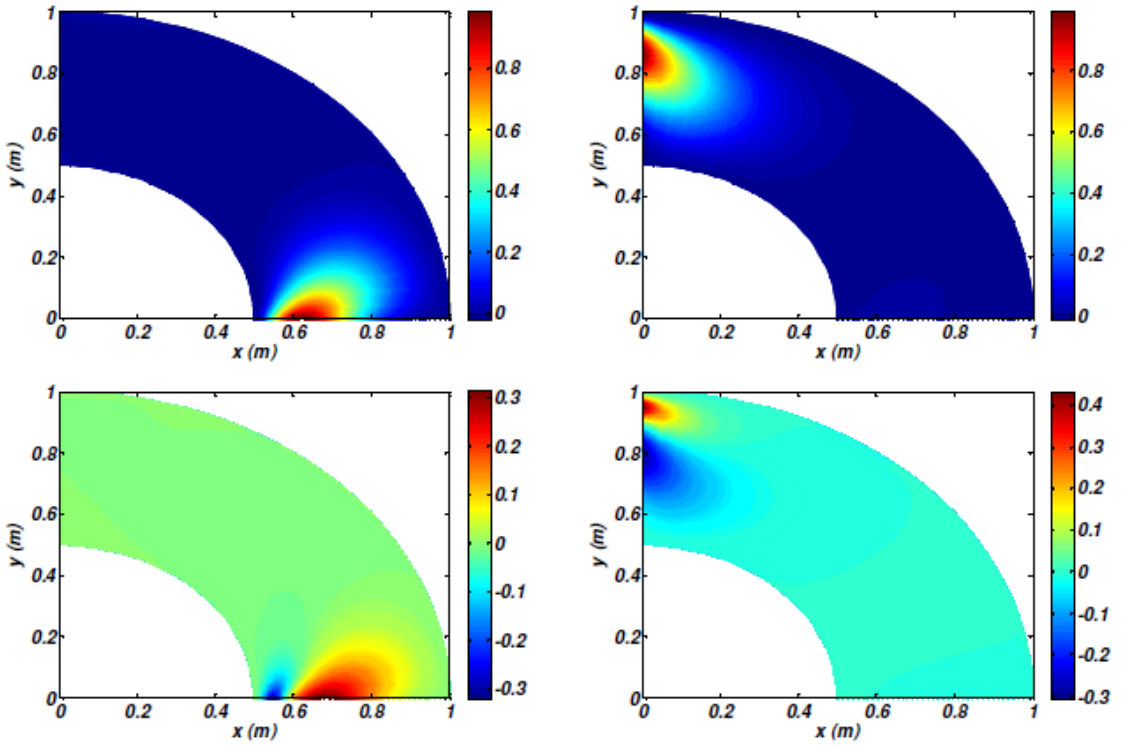

Fig 4: The first four shear mode shapes of FG porous annular sector plate reinforced by graphene platelet (a=0.5m, b=1m and h=0.1m, e_0=0.5, GPL-X, $\beta = 90^{\circ}, \gamma = 0.01\% wt$,PD1 ,B.C.2

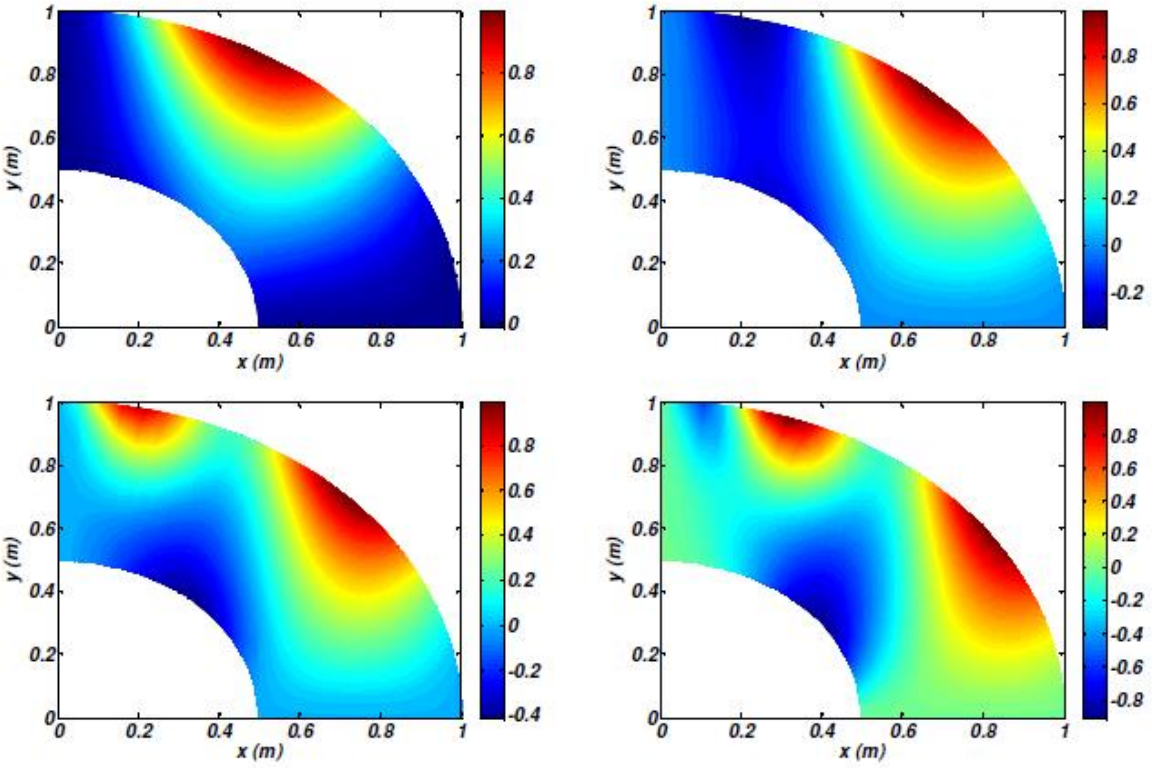

Fig 5: The first four shear mode shapes of FG porous annular sector plate reinforced by graphene platelet (B.C.3) (a=0.5 m, b=1 m and h=0.1 m ,e0=0.5,GPL-X, $\beta = 90^{\circ}, \gamma = 0.01\% wt$,PD1 ,B.C.3)

4. Conclusion

Shear buckling analysis of FG porous annular sector plate reinforced by graphene platelets based on 3D elasticity theory has been investigated for the first time. The Finite element method in conjunction with generalized geometric stiffness concept and the principle of minimum total potential energy utilized to derive and solve the governing equations. The influences various parameters including porosity coefficient, porosity distributions, GPL dispersion pattern, weight fraction of nanoffilers, sector angle and different boundary conditions on shear buckling loads of annular sector plate have been examined. Some of main results of present study are:

a) Maximum and minimum shear buckling loads are related to GPL-X and GPL-UD, respectively. Its difference is approximately 22%
b) The critical shear buckling loads for GPL-A and GPL-V are almost the same.
c) The maximum and minimum buckling loads belong to PD1 and PD3. Its difference is lower than 10%.
d) By increasing the weight fraction of GPLs, the shear buckling loads of the structure considerably increase (approximately 33%).
e) The influence of porosity coefficient on the critical shear buckling loads of the FG-GPL porous annular sector is lower than other parameters

5. References

[1] L. Hromadová, Thermal pressurization of pore fluid during earthquake slip, *Comenius University, Bratislava*, 2009.
[2] M. A. Biot, Theory of elasticity and consolidation for a porous anisotropic solid, *Journal of applied physics*, Vol. 26, No. 2, pp. 182-185, 1955.
[3] I. Gibson, M. F. Ashby, The mechanics of three-dimensional cellular materials, *Proceedings of the royal society of London. A. Mathematical and physical sciences*, Vol. 382, No. 1782, pp. 43-59, 1982.
[4] M. F. Ashby, A. Evans, N. Fleck, L. Gibson, J. Hutchinson, H. Wadley, F. Delale, Metal foams: a design guide, *Appl. Mech. Rev.*, Vol. 54, No. 6, pp. B105-B106, 2001.
[5] J. Choi, R. Lakes, Analysis of elastic modulus of conventional foams and of re-entrant foam materials with a negative Poisson's ratio, *International Journal of Mechanical Sciences*, Vol. 37, No. 1, pp. 51-59, 1995.
[6] M. Babaei, F. Kiarasi, K. Asemi, M. Hosseini, Functionally graded saturated porous structures: A review, *Journal of Computational Applied Mechanics*, Vol. 53, No. 2, pp. 297-308, 2022.
[7] M. Babaei, F. Kiarasi, K. Asemi, R. Dimitri, F. Tornabene, Transient thermal stresses in FG porous rotating truncated cones reinforced by graphene platelets, *Applied Sciences*, Vol. 12, No. 8, pp. 3932, 2022.
[8] M. Babaei, M. H. Hajmohammad, K. Asemi, Natural frequency and dynamic analyses of functionally graded saturated porous annular sector plate and cylindrical panel based on 3D elasticity, *Aerospace Science and Technology*, Vol. 96, pp. 105524, 2020.
[9] M. Babaei, K. Asemi, Stress analysis of functionally graded saturated porous rotating thick truncated cone, *Mechanics Based Design of Structures and Machines*, Vol. 50, No. 5, pp. 1537-1564, 2022.
[10] M. Babaei, K. Asemi, F. Kiarasi, Dynamic analysis of functionally graded rotating thick truncated cone made of saturated porous materials, *Thin-Walled Structures*, Vol. 164, pp. 107852, 2021.
[11] M. Mohammadi, A. Farajpour, A. Moradi, M. Hosseini, Vibration analysis of the rotating multilayer piezoelectric Timoshenko nanobeam, *Engineering Analysis with Boundary Elements*, Vol. 145, pp. 117-131, 2022.
[12] M. Mohammadi, A. Rastgoo, Primary and secondary resonance analysis of FG/lipid nanoplate with considering porosity distribution based on a nonlinear elastic medium, *Mechanics of Advanced Materials and Structures*, Vol. 27, No. 20, pp. 1709-1730, 2020.
[13] M. Mohammadi, M. Hosseini, M. Shishesaz, A. Hadi, A. Rastgoo, Primary and secondary resonance analysis of porous functionally graded nanobeam resting on a nonlinear foundation subjected to mechanical and electrical loads, *European Journal of Mechanics-A/Solids*, Vol. 77, pp. 103793, 2019.
[14] M. Mohammadi, M. Safarabadi, A. Rastgoo, A. Farajpour, Hygro-mechanical vibration analysis of a rotating viscoelastic nanobeam embedded in a visco-Pasternak elastic medium and in a nonlinear thermal environment, *Acta Mechanica*, Vol. 227, pp. 2207-2232, 2016.
[15] M. Mohammadi, M. Ghayour, A. Farajpour, Free transverse vibration analysis of circular and annular graphene sheets with various boundary conditions using the nonlocal continuum plate model, *Composites Part B: Engineering*, Vol. 45, No. 1, pp. 32-42, 2013.

[16] M. Mohammadi, M. Goodarzi, M. Ghayour, A. Farajpour, Influence of in-plane pre-load on the vibration frequency of circular graphene sheet via nonlocal continuum theory, *Composites Part B: Engineering*, Vol. 51, pp. 121-129, 2013.

[17] M. Mohammadi, M. Ghayour, A. Farajpour, Using of new version integral differential method to analysis of free vibration orthotropic sector plate based on elastic medium, in *Proceeding of*, www.civilica.com/Paper-ISME19-ISME19_497.html, pp. 497.

[18] M. Mohammadi, A. Farajpour, A. Rastgoo, Coriolis effects on the thermo-mechanical vibration analysis of the rotating multilayer piezoelectric nanobeam, *Acta Mechanica*, Vol. 234, No. 2, pp. 751-774, 2023/02/01, 2023.

[19] F. Kiarasi, M. Babaei, K. Asemi, R. Dimitri, F. Tornabene, Three-dimensional buckling analysis of functionally graded saturated porous rectangular plates under combined loading conditions, *Applied Sciences*, Vol. 11, No. 21, pp. 10434, 2021.

[20] M. Babaei, K. Asemi, P. Safarpour, Buckling and static analyses of functionally graded saturated porous thick beam resting on elastic foundation based on higher order beam theory, *Iranian Journal of Mechanical Engineering Transactions of the ISME*, Vol. 20, No. 1, pp. 94-112, 2019.

[21] E. Magnucka-Blandzi, Axi-symmetrical deflection and buckling of circular porous-cellular plate, *Thin-walled structures*, Vol. 46, No. 3, pp. 333-337, 2008.

[22] M. Jabbari, A. Mojahedin, M. Haghi, Buckling analysis of thin circular FG plates made of saturated porous-soft ferromagnetic materials in transverse magnetic field, *Thin-Walled Structures*, Vol. 85, pp. 50-56, 2014.

[23] A. Mojahedin, M. Jabbari, M. Salavati, Axisymmetric buckling of saturated circular porous-cellular plate based on first-order shear deformation theory, *International Journal of Hydromechatronics*, Vol. 2, No. 4, pp. 144-158, 2019.

[24] A. Mojahedin, M. Jabbari, A. Khorshidvand, M. Eslami, Buckling analysis of functionally graded circular plates made of saturated porous materials based on higher order shear deformation theory, *Thin-Walled Structures*, Vol. 99, pp. 83-90, 2016.

[25] A. Rezaei, A. Saidi, Buckling response of moderately thick fluid-infiltrated porous annular sector plates, *Acta Mechanica*, Vol. 228, pp. 3929-3945, 2017.

[26] E. S. Rad, A. Saidi, A. Rezaei, M. Askari, Shear deformation theories for elastic buckling of fluid-infiltrated porous plates: an analytical approach, *Composite Structures*, Vol. 254, pp. 112829, 2020.

[27] E. Arshid, S. Amir, A. Loghman, Bending and buckling behaviors of heterogeneous temperature-dependent micro annular/circular porous sandwich plates integrated by FGPEM nano-Composite layers, *Journal of Sandwich Structures & Materials*, Vol. 23, No. 8, pp. 3836-3877, 2021.

[28] M. H. Sharifan, M. Jabbari, Mechanical buckling analysis of saturated porous functionally graded elliptical plates subjected to in-plane force resting on two parameters elastic foundation based on HSDT, *Journal of Pressure Vessel Technology*, Vol. 142, No. 4, pp. 041302, 2020.

[29] Z. Zhou, Y. Ni, Z. Tong, S. Zhu, J. Sun, X. Xu, Accurate nonlinear buckling analysis of functionally graded porous graphene platelet reinforced composite cylindrical shells, *International Journal of Mechanical Sciences*, Vol. 151, pp. 537-550, 2019.

[30] D. Shahgholian-Ghahfarokhi, G. Rahimi, A. Khodadadi, H. Salehipour, M. Afrand, Buckling analyses of FG porous nanocomposite cylindrical shells with graphene platelet reinforcement subjected to uniform external lateral pressure, *Mechanics Based Design of Structures and Machines*, Vol. 49, No. 7, pp. 1059-1079, 2021.

[31] D. Shahgholian-Ghahfarokhi, M. Safarpour, A. Rahimi, Torsional buckling analyses of functionally graded porous nanocomposite cylindrical shells reinforced with graphene platelets (GPLs), *Mechanics Based Design of Structures and Machines*, Vol. 49, No. 1, pp. 81-102, 2021.

[32] J. Yang, D. Chen, S. Kitipornchai, Buckling and free vibration analyses of functionally graded graphene reinforced porous nanocomposite plates based on Chebyshev-Ritz method, *Composite Structures*, Vol. 193, pp. 281-294, 2018.

[33] Y. Dong, L. He, L. Wang, Y. Li, J. Yang, Buckling of spinning functionally graded graphene reinforced porous nanocomposite cylindrical shells: An analytical study, *Aerospace Science and Technology*, Vol. 82, pp. 466-478, 2018.

[34] R. Ansari, R. Hassani, R. Gholami, H. Rouhi, Nonlinear bending analysis of arbitrary-shaped porous nanocomposite plates using a novel numerical approach, *International Journal of Non-Linear Mechanics*, Vol. 126, pp. 103556, 2020.

[35] S. Kitipornchai, D. Chen, J. Yang, Free vibration and elastic buckling of functionally graded porous beams reinforced by graphene platelets, *Materials & Design*, Vol. 116, pp. 656-665, 2017.

[36] C. Twinkle, J. Pitchaimani, Free vibration and stability of graphene platelet reinforced porous nano-composite cylindrical panel: Influence of grading, porosity and non-uniform edge loads, *Engineering Structures*, Vol. 230, pp. 111670, 2021.

[37] Q. H. Nguyen, L. B. Nguyen, H. B. Nguyen, H. Nguyen-Xuan, A three-variable high order shear deformation theory for isogeometric free vibration, buckling and instability analysis of FG porous plates reinforced by graphene platelets, *Composite Structures*, Vol. 245, pp. 112321, 2020.

[38] M. R. Anamagh, B. Bediz, Free vibration and buckling behavior of functionally graded porous plates reinforced by graphene platelets using spectral Chebyshev approach, *Composite Structures*, Vol. 253, pp. 112765, 2020.

[39] H. Yaghoobi, F. Taheri, Analytical solution and statistical analysis of buckling capacity of sandwich plates with uniform and non-uniform porous core reinforced with graphene nanoplatelets, *Composite Structures*, Vol. 252, pp. 112700, 2020.

[40] G. R. Asgari, A. Arabali, M. Babaei, K. Asemi, Dynamic instability of sandwich beams made of isotropic core and functionally graded graphene platelets-reinforced composite face sheets, *International Journal of Structural Stability and Dynamics*, Vol. 22, No. 08, pp. 2250092, 2022.

[41] M. Babaei, F. Kiarasi, M. S. Tehrani, A. Hamzei, E. Mohtarami, K. Asemi, Three dimensional free vibration analysis of functionally graded graphene reinforced composite laminated cylindrical panel, *Proceedings of the Institution of Mechanical Engineers, Part L: Journal of Materials: Design and Applications*, Vol. 236, No. 8, pp. 1501-1514, 2022.

[42] M. Khatounabadi, M. Jafari, K. Asemi, Low-velocity impact analysis of functionally graded porous circular plate reinforced with graphene platelets, *Waves in Random and Complex Media*, pp. 1-27, 2022.

[43] F. Kiarasi, A. Asadi, M. Babaei, K. Asemi, M. Hosseini, Dynamic analysis of functionally graded carbon nanotube (FGCNT) reinforced composite beam resting on viscoelastic foundation subjected to impulsive loading, *Journal of Computational Applied Mechanics*, Vol. 53, No. 1, pp. 1-23, 2022.

[44] M. Babaei, K. Asemi, F. Kiarasi, Static response and free-vibration analysis of a functionally graded annular elliptical sector plate made of saturated porous material based on 3D finite element method, *Mechanics Based Design of Structures and Machines*, pp. 1-25, 2020.

[45] R. Mahmoudi, A. Barati, M. Hosseini, A. Hadi, Torsional vibration of functionally porous nanotube based on nonlocal couple stress theory, *International Journal of Applied Mechanics*, Vol. 13, No. 10, pp. 2150122, 2021.

[46] E. Sobhani, A. R. Masoodi, R. Dimitri, F. Tornabene, Free vibration of porous graphene oxide powder nano-composites assembled paraboloidal-cylindrical shells, *Composite Structures*, Vol. 304, pp. 116431, 2023.

[47] M. R. Eslami, M. R. Eslami, Finite Element of Elastic Membrane, *Finite Elements Methods in Mechanics*, pp. 35-55, 2014.